CrossMark

ORIGINAL PAPER

Formation of Copper–Nickel Alloy from Their Oxide Mixtures Through Reduction by Low-Temperature Hydrogen Plasma

Kali Charan Sabat[1,2,3] · Raja Kishore Paramguru[3] ·
Barada Kanta Mishra[2,4]

Abstract The paper presents experimental results of a new method of production of nanoparticles of copper–nickel alloys from the reduction of the mixture of cupric oxide (CuO) and nickel oxide (NiO) by low-temperature hydrogen plasma in a microwave assisted hydrogen plasma set-up. The microwave power and hydrogen flow-rate used for the current investigation are 750 W and 2.5×10^{-6} m^3 s^{-1} respectively. The addition of NiO–CuO, in proportion to result in alloys of 90Cu:10Ni and 70Cu:30Ni, not only removed the induction period from the kinetic plot of CuO reduction but also, improved the reduction rate of CuO. The XRD analysis of the product exhibited a single-phase peak with a d-spacing lying between Cu and Ni, which satisfies the Vergard's law, indicating the Cu–Ni alloy formation. The lattice parameter decreases from 3.6221 (90Cu:10Ni) to 3.595 Å (70Cu:30Ni), due to the smaller atomic radius of Ni (0.1246 nm) than that of Cu (0.1278 nm). The crystallite size, calculated by applying Scherrer's formula, in both cases is found to be 31.7 nm.

Keywords Cu–Ni alloy · Low-temperature hydrogen plasma · Reduction of metal oxides · Vergard's law · Nanoparticles

✉ Barada Kanta Mishra
  bkm.immt@gmail.com

[1] Parala Maharaja Engineering College (A Constituent College of BPUT, Odisha), Sitalapalli, Brahmapur, Odisha 761003, India

[2] CSIR-Institute of Minerals and Materials Technology, Bhubaneswar, Odisha 751013, India

[3] KIIT University, Bhubaneswar, Odisha 751024, India

[4] Indian Institute of Technology, Goa, Goa Engineering College Campus, Farmagudi, Ponda, Goa 403401, India

Introduction

Copper–Nickel alloys are being used in different industries due to improved properties like mechanical, corrosion resistant, electrical, and thermal conductivity. They are widely used in condensers, heat exchangers, corrosion resistant pipes, pumps and machineries, etc. [1–3]. These alloys are prepared by different methods [2–15]. The most commonly used method is to cast the mixture of molten copper and nickel or to sinter their well-mixed metal powders as practiced in powder metallurgy route [12–15]. The cast alloys of Cu–Ni are standardized according to EN 1982. The better known alloys in this standard (EN 1982) correspond to the alloy compositions of 90Cu:10Ni and 70Cu:30Ni. These alloys are generally prepared by casting of their molten metal mixtures. The production of alloys by direct reduction from a mixture of metal oxides, is a new concept [16]. In the present investigation, these alloy compositions of Cu and Ni were made directly from their metal oxide mixtures by reduction using low temperature hydrogen plasma.

Reduction of metal oxide in hydrogen plasma is a novel concept, and of late, reduction is made possible using low-temperature hydrogen plasma (LTHP) [16–21]. It has been found that during reduction of metal oxide by LTHP, the associated activation energy decreases due to the presence of excited species in LTHP. Further, the equilibrium partial pressure of atomic hydrogen needed to reduce the metal oxide goes down at low temperature unlike the corresponding reduction by molecular hydrogen. The LTHP can be employed for production of alloys by reduction of the corresponding metal oxide mixtures. Literature show that FeCo alloy [16] could be produced but FeCu alloy could not be produced by similar approach, instead, Fe and Cu metallic mixtures could be produced from the reduction of their oxide mixtures by LTHP [16]. Formation of FeNi alloy has also been produced from the mixture of Fe_2O_3 and NiO [22].

There are two different kinetic models used to describe the reduction of metal oxides by molecular hydrogen: interface-controlled and nucleation-growth model. The nucleation and growth process exhibit an induction period followed by autocatalysis [23–30]. The induction period has already been reported during reduction by molecular hydrogen for reduction of hematite [23], magnetite [24, 25], nickel oxide [26–28] and copper oxide [30]. The removal of induction period during reduction of NiO by LTHP has already been reported [22]. But the induction period in case of CuO [20] couldn't be removed even with LTHP.
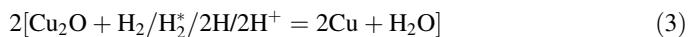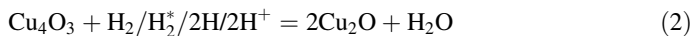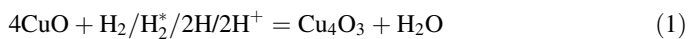
The present investigation is about reduction of mixture of NiO and CuO by LTHP. This approach was undertaken due to the following favorable facts: (a) individual oxide reduction of CuO and NiO can be achieved, (b) induction period in case of CuO cannot be removed even with excited species of hydrogen plasma, though it can be removed in case of NiO, (c) Cu–Ni alloys satisfy the Hume-Rothery rules of substitutional isomorphous solid solutions due to their similar crystal structure, similar atomic radius, electronegativity, and valency [31, 32]. Considering all these facts, the oxide mixtures corresponding to alloy compositions of 90Cu:10Ni and 70Cu:30Ni have been investigated.

Thermodynamics provides the potential pathways for reduction of metal oxides to metals [17]. So, the thermodynamic feasibility of reduction of CuO $\rightarrow$ Cu and NiO $\rightarrow$ Ni by molecular hydrogen has been estimated by their Gibb's standard free energy (ΔG^0) at various temperatures, which is shown in Fig. 1. The ΔG^0 values of the reduction reactions CuO $\rightarrow$ Cu and NiO $\rightarrow$ Ni is negative at all temperatures, indicating the thermodynamic feasibility of molecular hydrogen to reduce these oxides at all temperatures. The LTHP produced at the pellet interface consists of various excited species such as ro-vibrationally excited hydrogen molecules (H^*_2), atomic hydrogen (H) and ionic hydrogen (H+). These
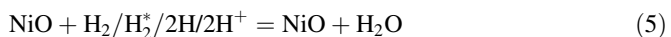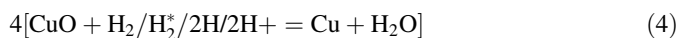
Fig. 1 Ellingham diagram for CuO, 90Cu–10Ni, 70Cu–30Ni, NiO, HP–90Cu–10Ni and HP–70Cu–30Ni
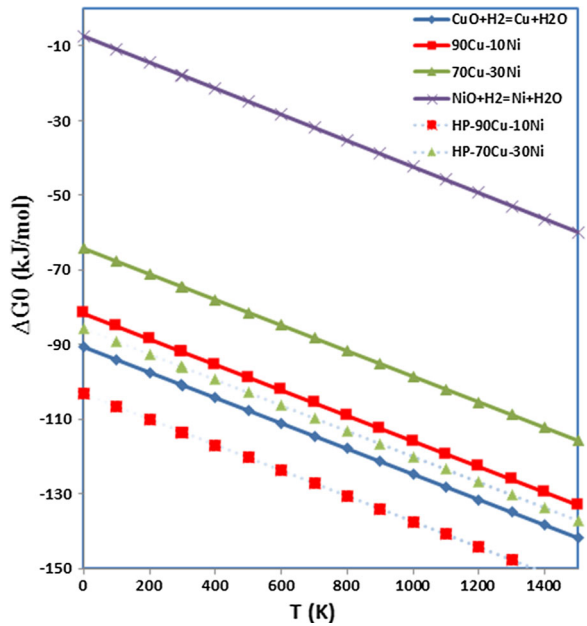
excited species lower the ΔG^0 values below the molecular hydrogen line. Specifically, the H_2^* molecules have lower ΔG^0 than the molecular hydrogen; H and H^+ decrease the ΔG^0 by more than 600 and 6000 kJ/mol, respectively [17, 20]. The presence of these excited species in LTHP reduces the ΔG^0 values suggesting that hydrogen in plasma state is more potent than molecular hydrogen as reductant. In a microwave assisted setup under similar operating conditions as in the present investigation, Hassouni et al. [33] reported LTHP consisting of 2% H, 8% H_2^* (v = 1 level) and 90% H_2. The additional energy due to these excited species was estimated as 21.5 kJ/mol [21]. The ΔG^0 calculated after adding this additional energy for LTHP is shown as dotted lines in Fig. 1. This additional energy decreases the ΔG^0 value of molecular hydrogen. The decrease in ΔG^0 gives the advantage in favor of LTHP. Depending on the reaction conditions employed, a number of pathways exists for reduction of CuO and NiO [28–30]. In the presence of LTHP, the reduction proceeds through the following reactions steps [17, 20]:

$$4CuO + H_2/H_2^*/2H/2H^+ = Cu_4O_3 + H_2O \tag{1}$$

$$Cu_4O_3 + H_2/H_2^*/2H/2H^+ = 2Cu_2O + H_2O \tag{2}$$

$$2[Cu_2O + H_2/H_2^*/2H/2H^+ = 2Cu + H_2O] \tag{3}$$

The overall reaction is

$$4[CuO + H_2/H_2^*/2H/2H+ = Cu + H_2O] \tag{4}$$

$$NiO + H_2/H_2^*/2H/2H^+ = NiO + H_2O \tag{5}$$

Bauer–Glaessner diagram (Fig. 2) was drawn for the above intermediate products by using their thermodynamic properties. However, the Bauer–Glaessner diagram for the
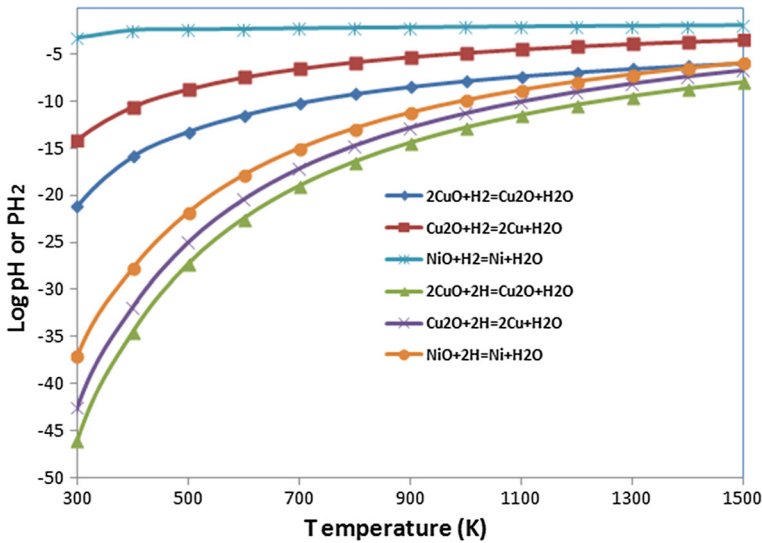
Fig. 2 Bauer–Glaessner diagram variation in hydrogen partial pressure with temperature

reaction $Cu_4O_3 + H_2 = 2Cu_2O + H_2O$, couldn't be drawn due to the unavailability of thermodynamic data for Cu_4O_3. Figure 2 provides interesting and meaningful inferences. The partial pressure of H_2/H required for reduction of all oxides of copper and nickel decreases with a decrease in temperature. The decrease is much sharper for atomic hydrogen. The LTHP consists of 2% H, 8% H^*_2 (v = 1 level) and 90% H_2, So, the decrease in partial pressure of LTHP is expected to come in between the molecular hydrogen and atomic hydrogen. Thus, a lower temperature is more favorable for reduction by atomic hydrogen, which is highly significant for the reduction of the oxides of copper and nickel by LTHP.

Both Ellingham diagram and Bauer–Glaessner diagram show favourable conditions for the reduction of copper oxides and nickel oxide with respect to molecular hydrogen for reduction. The remarkable fact is that the atomic hydrogen line is very much below the copper oxide and nickel oxide lines. The difference is more than 1000 and 600 kJ at all temperatures for copper oxide and nickel oxide respectively. These values indicate that the atomic hydrogen is a very strong reductant for copper oxides and nickel oxide, in comparison to molecular hydrogen. The strength of ionic hydrogen as a reductant is still much more. The lines for the excited hydrogen molecules is expected to lie between the molecular and atomic hydrogen lines suggesting that it is a stronger reductant than molecular hydrogen. The Ellingham diagram is supported by the Bauer–Glaessner diagram, due to the fact that the partial pressure of molecular hydrogen required for reduction decreases with decrease in temperature, as shown in Fig. 2.

Experimental Details

The experimental details pertaining to the metal oxides, preparation of compacted pellets from these metal oxides, the experimental set-up and procedure, material (raw-material and products) characterization methods, etc., are presented elsewhere in detail [16–21]. The

CuO and NiO samples used in this study were sourced from J.T. Baker Ltd. An X'Pert PRO-PANalytical model no. 3040160 was used for X-ray diffraction (XRD) of these raw powders, and the studies of the different phases in the reduced samples. The XRD plot of the raw material CuO is shown in Fig. 3 and the XRD of NiO sample is shown in Fig. 4. It was found from XRD analysis that the major constituent present in the cupric oxide sample is CuO with traces of Cu_4O_3 as per JCPDS file nos. 98-002-8583 and 98-006-2016 respectively [20]. The 2θ values and intensities for the JCPDS files of Cu_4O_3 and Cu_2O are shown in Table 1, as an aid to the reader when viewing the XRD spectra presented in Fig. 8a–c. The XRD analysis of nickel oxide showed only NiO as per JCPDS file no. 00-044-1159.

The microwave plasma reactor supplied by IMAT Pvt. Ltd., India, incorporates a power supply of 6000 W and a microwave generator (2.45×10^9 Hz) to produce plasma at high power densities. The high-frequency microwaves interact with the hydrogen gas available inside the system to produce hydrogen plasma. The sample placed on a molybdenum sample holder is in turn placed at the centre of the reaction chamber within the plasma range. The microwave power and hydrogen flow rate were kept constant and monitored throughout the experiments. Likewise, the temperature and pressure were properly monitored throughout the experiments. The reduction experiments were carried out for different time periods till complete reduction. Weight loss measurements were carried out to determine the percentage reductions for each time period with a digital weighing balance with accuracy 0.1×10^{-6} kg. All the experiments were carried out at a flow rate of 2.5×10^{-6} m^3 s^{-1} and operating pressure 1.719×10^{-3} Pa.

Results and Discussion

Reduction Studies

The reduction studies of the oxide mixtures were carried out by mixing the oxide mixtures in appropriate proportions to give rise to the desired alloy composition of 90Cu:10Ni and 70Cu:30Ni after reduction. All the experiments were carried out at microwave power of 750 W and flow rate of 2.5×10^{-6} m^3 s^{-1} for different time periods. The experimental
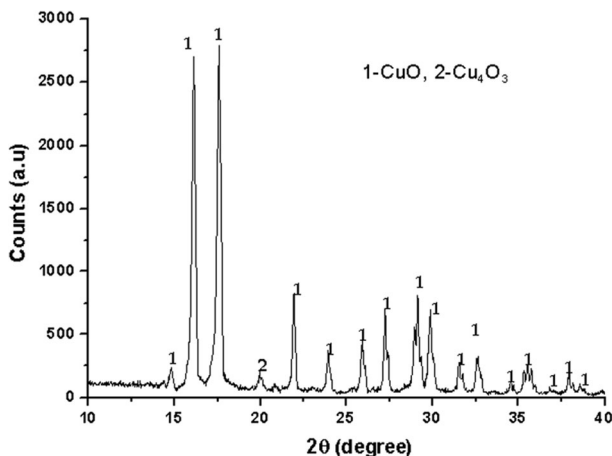

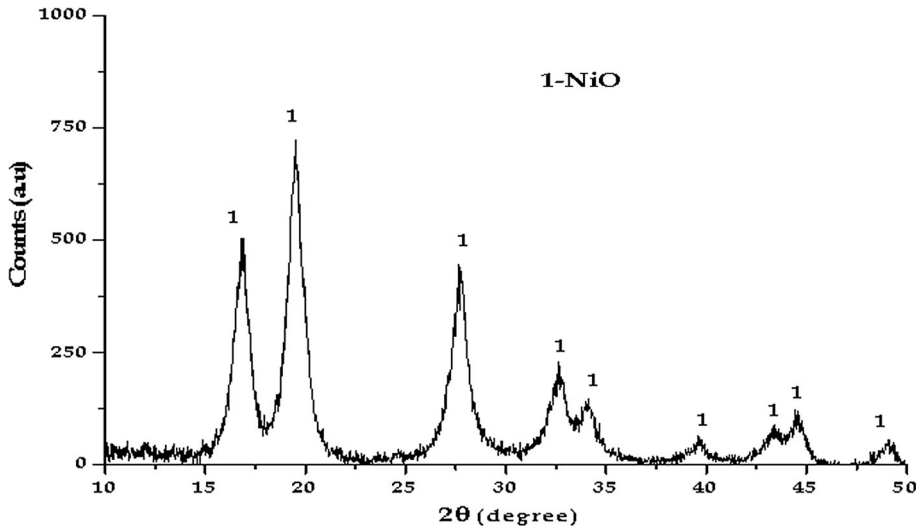**Fig. 3** XRD of raw material of copper oxide

Fig. 4 XRD of raw material of nickel oxide

Table 1 The 2θ values and intensities of the JCPDS files of Cu$_2$O—JCPDS 98-002-1472 and Cu$_4$O$_3$—JCPDS 98-006-2016

Cu$_2$O—JCPDS 98-002-1472		Cu$_4$O$_3$—JCPDS 98-006-2016	
2θ values	Intensities	2θ values	Intensities
16.554	100.0	16.262	100.0
19.138	36.4	16.487	15.6
27.194	32.3	19.857	18.0
32.004	27.0	25.917	28.2
		28.627	13.9

results of reduction for 90Cu:10Ni and 70Cu:30Ni are shown in Table 1. The corresponding variations in pressure and temperature with time are shown in Fig. 5a, b. As depicted by the Ellingham diagram and B–G diagram, good reduction of CuO, 90Cu:10Ni and 70Cu:30Ni was observed (Table 2).

The reduction rate plots are shown in Fig. 6. For the sake of comparison, the plot of reduction of CuO under these conditions, as reported in the earlier publication [20] is also placed in Fig. 6. As evident from Fig. 6, with the addition of NiO, the induction period observed in the reduction plot of CuO is vanished. Also, the percentage reduction increased for a particular time period of reduction, with the addition of NiO.

The overall reduction of CuO takes place in the sequence CuO → Cu$_4$O$_3$ → Cu$_2$O → Cu, and the rate plot of CuO is close to a sigmoidal plot. The nature of these plots were explained by nucleation and grain-growth model [20, 23–30, 34], represented by the rate equation:

$$[-\ln(1-a)]^{1/n} = k_{app} \cdot t$$

where, α is the percent reduction (in percentage), t is the time of reduction (in s), k_{app} is the apparent rate constant (in s^{-1}), and n is the Avrami parameter. The n value for the CuO reduction was found to be closer to 3 [20]. The plot for CuO reduction in conditions similar
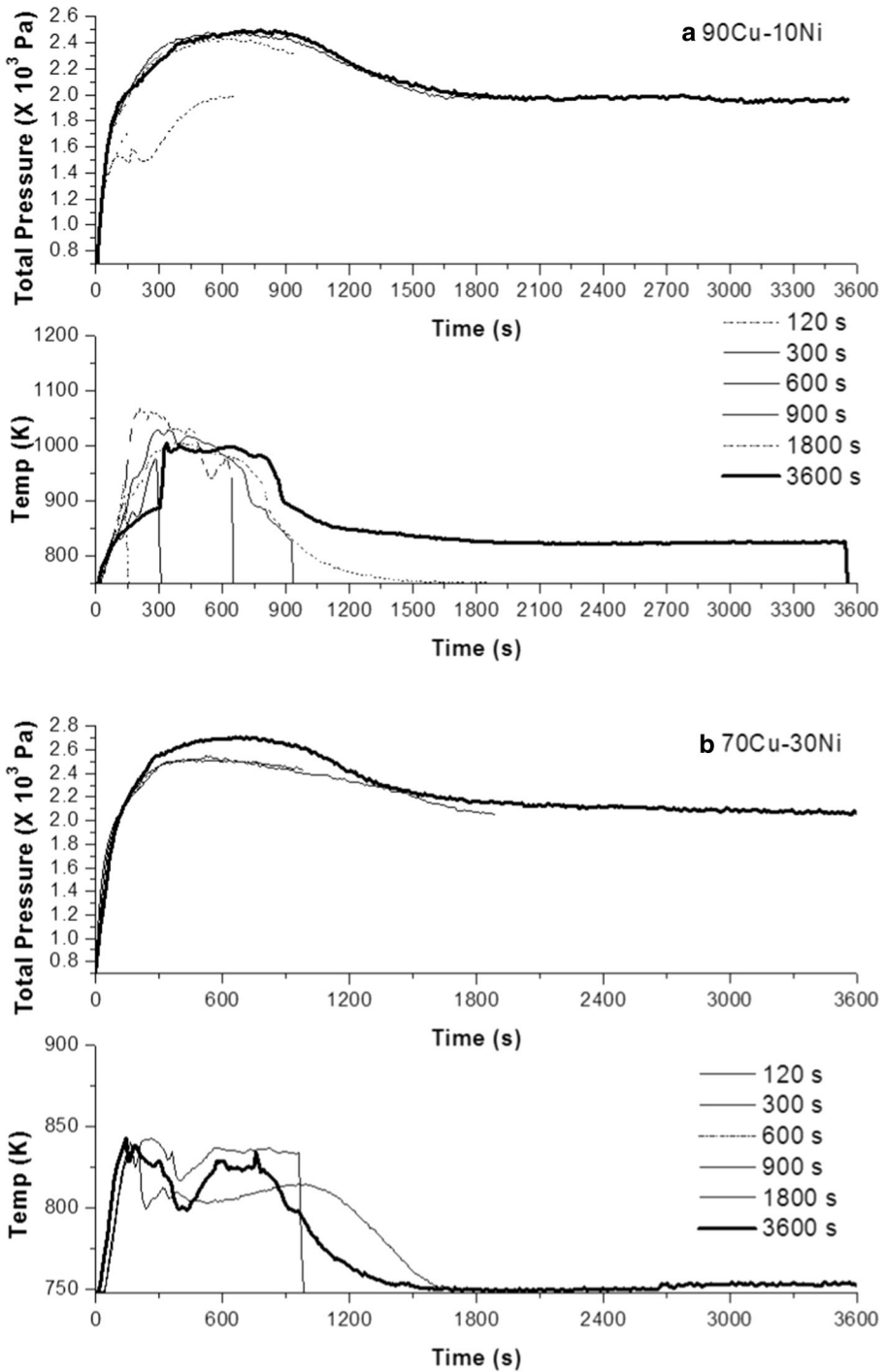
Fig. 5 Variation of interface temperature and pressure for **a** 90Cu:10Ni, **b** 70Cu:30Ni

Table 2 Experimental results of reduction of 90Cu:10Ni and 70Cu:30Ni by hydrogen plasma at microwave power 750 W and hydrogen flowrate 2.5×10^{-6} m^3 s^{-1}

Composition	Time/ s	Initial weight/ 10^{-3} kg	Final weight/ 10^{-3} kg	Weight loss/ 10^{-3} kg	Reduction/ %
90Cu:10Ni	120	2.3150	2.2661	0.0489	10
90Cu:10Ni	300	2.4927	2.3299	0.1628	32
90Cu:10Ni	600	2.5159	2.1515	0.3644	70
90Cu:10Ni	900	2.5481	2.0878	0.4603	88
90Cu:10Ni	1800	2.4691	1.9510	0.5181	102
90Cu:10Ni	2700	2.4855	1.9730	0.5125	100
90Cu:10Ni	3600	2.5382	1.9992	0.5390	103
70Cu:30Ni	120	2.4721	2.3879	0.0842	17
70Cu:30Ni	300	2.5056	2.3429	0.1627	32
70Cu:30Ni	600	2.5930	2.2046	0.3884	74
70Cu:30Ni	900	2.5309	2.0531	0.4778	93
70Cu:30Ni	1800	2.5111	2.0049	0.5062	100
70Cu:30Ni	3600	2.5512	2.0271	0.5241	101
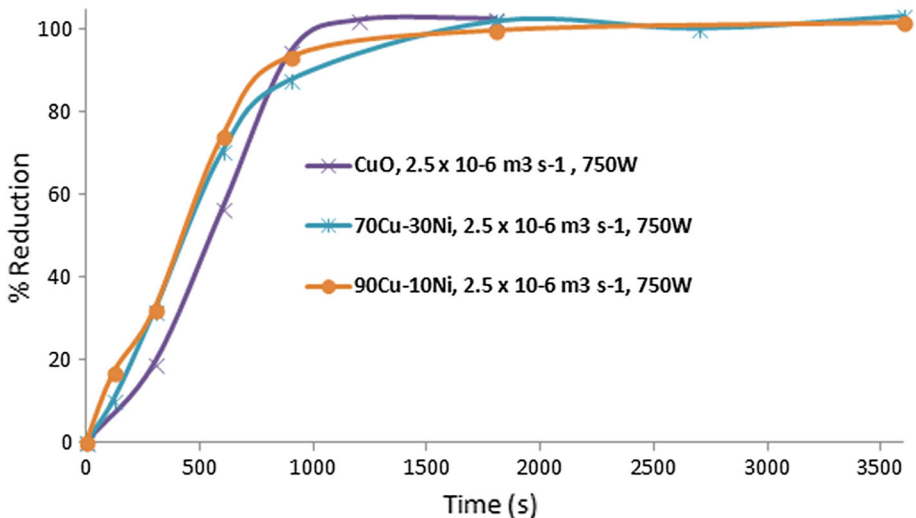
Fig. 6 Plot of percentage reduction for various times for CuO, 90Cu:10Ni and 70Cu:30Ni

to the present one has been reproduced in Fig. 7. The rate plots of reduction of the oxide mixtures aiming at 70Cu:30Ni 70%Cu–30%Ni as well as 90Cu:10Ni are also presented in Fig. 7. It can be seen that these are straight line plots, but with a slope closer to 1 (indicative of first order reaction) instead of 3 (indicative of nucleation and grain-growth model) as found for the CuO reduction kinetics. It has been reported earlier that similar to the induction period observed during the reduction of CuO by atmospheric hydrogen gas, an induction period do exists for the reduction of NiO by hydrogen [26–28] which vanishes
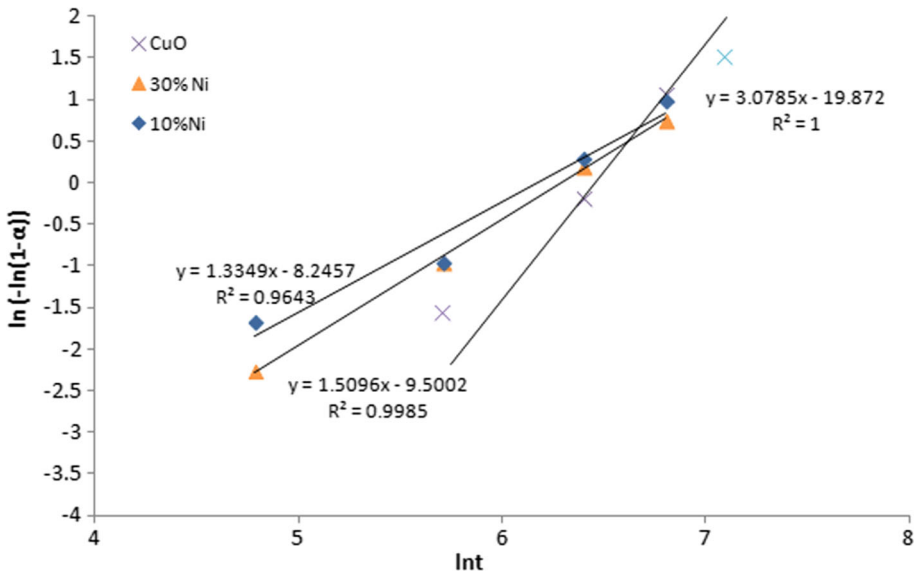
Fig. 7 Rate plots for reduction of CuO, 90Cu:10Ni and 70Cu:30Ni following Johnson Mehl equation

at higher temperature (above 310 °C). Here, addition of NiO has removed the induction period for CuO, besides enhancing the level of reduction of CuO. The temperature in this study was higher, and the entry of NiO into the CuO structure would have caused increase in 'O' vacancies as well as active sites to aid the reaction, thereby removing the induction period. Further, in this condition, NiO is reduced ahead of CuO resulting in significant contraction in the cell dimensions of NiO [26], thus allowing hydrogen to reach CuO easily.

XRD Analysis

The XRD analysis of the reduction products for CuO, 90Cu:10Ni, and 70Cu:30Ni are shown in Fig. 8a–c, respectively.

The XRD result of CuO has been reproduced in Fig. 8a, from the earlier publication [20], for comparison purpose. The transformation of CuO takes place in sequence $CuO \rightarrow Cu_4O_3 \rightarrow Cu_2O \rightarrow Cu$ [20]. It is a sigmoidal type nucleation and growth plot where the induction period is followed by auto-catalytic reduction. The predominant peaks observed during the induction period (300 and 600 s) are CuO and Cu_4O_3. These peaks almost diminish at 900 s. However, with the addition of NiO to CuO, for both compositions i.e., 90Cu:10Ni (Fig. 8b) and 70Cu:30Ni (Fig. 8c), the intensity of CuO and Cu_4O_3 peaks are reduced, and formation of Cu–Ni solid solution takes place even at 120 s. It implies that the addition of NiO not only eliminates the induction period observed during CuO reduction but also aids in Cu–Ni alloy formation during this period. At around 300 s, during the reduction of CuO, the XRD plot (Fig. 8a) starts showing the Cu peak. At 600 s, though the Cu peak intensity remains highest, the CuO and Cu_4O_3 peaks are still predominant. But with the addition of NiO, at 600 s, the intensities of CuO and Cu_4O_3 peaks significantly reduce as shown in Fig. 8b, c, implying that addition of NiO supports the complete reduction of CuO and formation of Cu–Ni solid solution. Interestingly, the X-ray
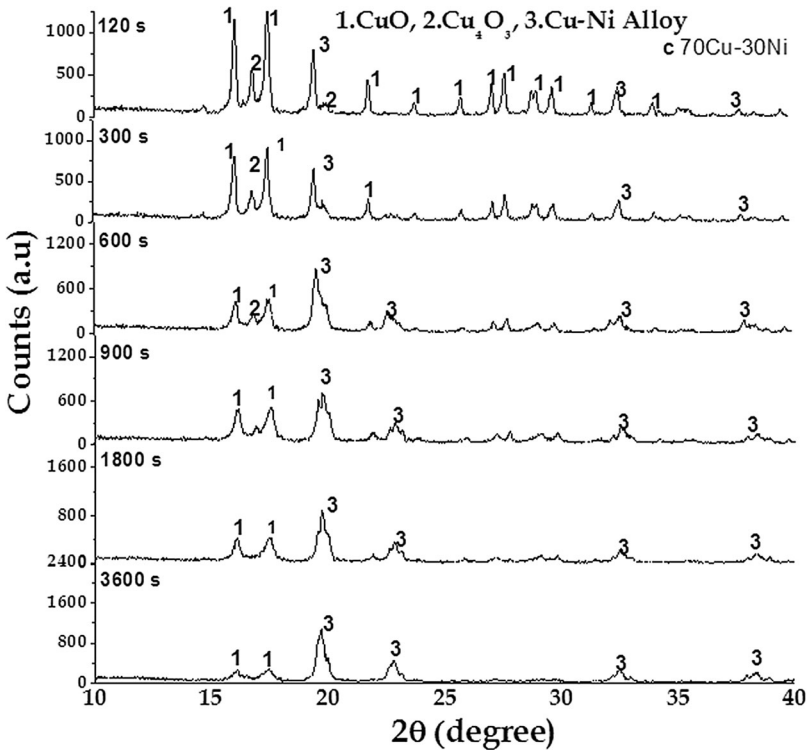
Fig. 8 XRD analysis of the reduction products for **a** CuO, **b** 90Cu:10Ni, **c** 70Cu:30Ni

Fig. 8 continued

analyses of 90Cu:10Ni (Fig. 8b) and 70Cu:30Ni (Fig. 8c) show a single-phase formation after around 1800 s, with traces of CuO. Single phase formation is the required condition for alloy formation. Also, the lattice constants for alloys calculated from Vergard's law should be equal to the additive values calculated from their mole fractions [35]. According to this law, unit cell parameters should vary linearly with composition for a continuous substitutional solid solution in which atoms or ions that substitute for each other are randomly distributed [35]. As mentioned earlier, Cu and Ni obey all the Hume-Rothery's rules of substitutional solid solubility. Both Cu and Ni are having the same crystal structure, so the diffracting planes are same. In order to verify the Vergard's law relation, the d-spacing values of the first 5 diffracting planes [(100), (200), (220), (311), (222)] are computed, and compared with the d-spacing values obtained experimentally for 90Cu:10Ni and 70Cu:30Ni. The values are shown in Table 3. The d-values obtained from experimental XRD patterns for both alloys, remain consistently slightly higher (0.1–0.4%) than the values calculated from Vergard's law. The d-values obtained from these alloys 90Cu:10Ni and 70Cu:30Ni, also remain little higher (0.4–0.8%) than the reported d-values for the 81Cu:19Ni composition, as reported in JCPDS file 00-007-1406. These higher d-values may be due to entrapment of H in the alloy. The entrapment of H has already been reported in the earlier publications [20, 26, 30]. Notwithstanding the minor deviations in d-values due to H entrapment, the estimated d-values matched well with the experimental values for both the alloys. So, it can easily be concluded that the experimental results

Table 3 d-Values obtained from experimental results and verification of Vergard's law

Sl. no.	Diff. plane	Cu: JCPDS file: d[Å] 00-004-0836: d[Å] (I)	Ni: JCPDS 00-004-0850: d[Å] (I)	81Cu-19Ni JCPDS 00-007-1406: d[Å] (I)	90Cu-10Ni From Vergard's law: d[Å]	90Cu-10Ni 30 min (Exp.): d[Å](I)	70Cu-30Ni from Vergard's law: d[Å] (I)	70Cu-30Ni 30 min (Exp.): d[Å] (I)
1	(111)	2.0880 (100)	2.0340 (100)	2.0740 (100)	2.0824	2.0913 (100)	2.0718	2.0756 (100)
2	(200)	1.8080 (46)	1.7620 (42)	1.7960 (50)	1.8034	1.8113 (40.91)	1.7942	1.7964 (39.33)
3	(220)	1.2780 (20)	1.2460 (21)	1.2700 (47)	1.2748	1.2785 (23.68)	1.2684	1.2689 (22.79)
4	(311)	1.0900 (17)	1.0620 (20)	1.0834 (30)	1.0872	1.0901 (20.35)	1.0817	1.0828 (14.63)
5	(222)	1.0436 (5)	1.0170 (7)	1.0373 (11)	1.0409	1.0443 (5.64)	1.0356	1.0322 (3.97)
Crystal size		3.6150	3.5238	3.5934	3.6067	3.6221	3.5883	3.5950
Crystallite size						31.7 nm		31.7 nm

follow the Vergard's law. The single-phase formation that obeys the Vergard's law prove the formation of a solid solution.

The d-value of the first five diffracting planes [(100), (200), (220), (311) and (222)] decreases with increasing Ni content from 90Cu:10Ni to 70Cu:30Ni of the Cu–Ni alloy, as shown in Table 3. This decline in d-value is due to the smaller atomic radius of Ni (0.1246 nm) compared to that of Cu (0.1278 nm). The smaller Ni atom when forms isomorphous solid solution with Cu, the d-value decreases. The lattice parameter measured from the experimental data of 90Cu:10Ni and 70Cu:30Ni decreases from 3.6221 to 3.595 Å. The lattice parameter calculated from Vergard's law also follows the same trend of reduction in the lattice parameter which decreases from 3.6067 to 3.5883 Å. The crystallite sizes of 90Cu:10Ni and 70Cu:30Ni has been estimated from Scherrer's formula [36–38]. The crystallite size in both cases is found to be 31.7 nm.

Another way to determine alloy formation is to examine the lattice strain from the broadening of XRD peak (FWHM) [36–38]. The lattice strain is calculated from the formula $\varepsilon = (\beta_r / 4 \tan\theta)$, where, ε is the lattice strain, β is the FWHM, and θ is the angle. Usually, β is obtained by eliminating the broadening due to the instrument from that measured by the following formula:

$[\beta = \sqrt{\{(\beta_{\text{ measured}})^2 - (\beta_{\text{ due to the instrument}})^2\}}]$; and ($\beta_{\text{ due to the instrument}}$) is determined using a well-annealed sample. However, in this study, the metallic Cu obtained after complete reduction of CuO was taken as the reference. Therefore, the FWHM was found to be higher than the FWHM measured using 90Cu:10Ni and 70Cu:30Ni samples. This may be due to the fact that the atomic radius of Ni is smaller (0.1246 nm) than that of Cu (0.1278 nm), and therefore, Ni is not expected to cause any lattice strain. Thus, FWHM values of Cu–Ni alloy are lower than that of pure Cu.

Conclusions

The following conclusions may be drawn from the present investigation for reduction of CuO and NiO mixtures:

1. The free energy values show that molecular hydrogen is a good reductant of both CuO and NiO. However, the H and H+ species present in hydrogen plasma can act as much stronger reductants.
2. The equilibrium partial pressure of H_2/H for reducing both CuO and NiO decrease with a decrease in temperature implying the possibility of low-temperature reduction of both oxides. In both cases, the decrease is much sharper for H, in comparison to H_2.
3. The addition of NiO not only eliminates the induction period, but also increases the reduction of oxide mixtures.
4. Cu–Ni single phase is formed satisfying the Vergard's law, which confirms the formation of Cu–Ni alloy.
5. The lattice parameter decreases from 3.6221 to 3.595 Å, due to the smaller atomic radius of Ni (0.1246 nm) than that of Cu (0.1278 nm). However, the crystallite size in both cases is found to be 31.7 nm.

References

1. Shams El Din AM, El Dahshan ME, Taj El Din AM (2000) Dissolution of copper and copper–nickel alloys in aerated dilute HCl solutions. Desalination 130:89–97. https://doi.org/10.1016/S0011-9164(00)00077-1
2. Jena PK, Brocchi EA, Motta MS (2004) Preparation of Cu–Ni alloys through a new chemical route. Metall Mater Trans B 35:1107–1112. https://doi.org/10.1007/s11663-004-0066-9
3. Ghosh SK, Grover AK, Dey GK, Totlani MK (2000) Nanocrystalline Ni–Cu alloy plating by pulse electrolysis. Surf Coat Technol 126:48–63. https://doi.org/10.1016/S0257-8972(00)00520-X
4. Chatterjee J, Bettge M, Haik Y, Jen Chen C (2005) Synthesis and characterization of polymer encapsulated Cu–Ni magnetic nanoparticles for hyperthermia applications. J Magn Magn Mater 293:303–309
5. Froes FH, Senkov ON, Baburaj EG (2001) Synthesis of nanocrystalline materials—an overview. Mater Sci Eng A 301:44–53. https://doi.org/10.1016/S0921-5093(00)01391-5
6. Kazeminezhad I, Schwarzacher W (2002) Studying the transition from multilayer to alloy in the Ni–Cu system. J Magn Magn Mater 240:467–468. https://doi.org/10.1016/S0304-8853(01)00900-3
7. Glibin VP, Kuznetsov BV, Vorobyova TN (2005) Investigation of the thermodynamic properties of Cu–Ni alloys obtained by electrodeposition or by casting. J Alloys Compd 386:139–143. https://doi.org/10.1016/j.jallcom.2004.05.052
8. Li YD, Li LQ, Liao HW, Wang HR (1999) Preparation of pure nickel, cobalt, nickel–cobalt and nickel–copper alloys by hydrothermal reduction. J Mater Chem 9:2675–2677. https://doi.org/10.1039/a904686k
9. Bonet F, Grugeon S, Dupont L et al (2003) Synthesis and characterization of bimetallic Ni–Cu particles. J Solid State Chem 172:111–115. https://doi.org/10.1016/S0022-4596(02)00163-9
10. Niu HL, Chen QW, Lin YS et al (2004) Hydrothermal formation of magnetic Ni–Cu alloy nanocrystallites at low temperatures. Nanotechnology 15:1054–1058. https://doi.org/10.1088/0957-4484/15/8/034
11. Rao GR, Mishra BG, Sahu HR (2004) Synthesis of CuO, Cu and CuNi alloy particles by solution combustion using carbohydrazide and N-tertiarybutoxy-carbonylpiperazine fuels. Mater Lett 58:3523–3527. https://doi.org/10.1016/j.matlet.2004.05.082
12. Davis JR (1998) Metals handbook. Met Handb. https://doi.org/10.1017/CBO9781107415324.004
13. Niu Y, Gesmundo F, Farnè G et al (2000) The air oxidation of a nanocrystalline Cu-10 wt%Ni alloy at 800 °C. Corros Sci 42:1763–1777. https://doi.org/10.1016/S0010-938X(00)00035-4
14. Agnew SR, Elliott BR, Youngdahl CJ et al (2000) Microstructure and mechanical behavior of nanocrystalline metals. Mater Sci Eng A 285:391–396. https://doi.org/10.1016/S0921-5093(00)00669-9
15. Durivault L, Brylev O, Reyter D et al (2007) Cu–Ni materials prepared by mechanical milling: their properties and electrocatalytic activity towards nitrate reduction in alkaline medium. J Alloys Compd 432:323–332. https://doi.org/10.1016/j.jallcom.2006.06.023
16. Sabat KC, Paramguru RK, Mishra BK (2017) Reduction of oxide mixtures of (Fe_2O_3 + CuO) and (Fe_2O_3 + Co_3O_4) by low-temperature hydrogen plasma. Plasma Chem Plasma Process 37:979–995. https://doi.org/10.1007/s11090-017-9818-6
17. Sabat KC, Rajput P, Paramguru RK et al (2014) Reduction of oxide minerals by hydrogen plasma: an overview. Plasma Chem Plasma Process 34:1–23. https://doi.org/10.1007/s11090-013-9484-2
18. Rajput P, Sabat KC, Paramguru RK et al (2014) Direct reduction of iron in low temperature hydrogen plasma. Ironmak Steelmak 41:721–731. https://doi.org/10.1179/1743281214Y.0000000186
19. Sabat KC, Paramguru RK, Pradhan S, Mishra BK (2015) Reduction of cobalt oxide (Co_3O_4) by low temperature hydrogen plasma. Plasma Chem Plasma Process 35:387–399. https://doi.org/10.1007/s11090-014-9602-9
20. Sabat KC, Paramguru RK, Mishra BK (2016) Reduction of copper oxide by low-temperature hydrogen plasma. Plasma Chem Plasma Process 36:1111–1124. https://doi.org/10.1007/s11090-016-9710-9
21. Sabat KC, Murphy AB (2017) Hydrogen plasma processing of iron ore. Metall Mater Trans B 48:1561–1594. https://doi.org/10.1007/s11663-017-0957-1
22. Rajput P, Bhoi B, Paramguru RK, Mishra BK (2016) Effect of plasma state and alloying addition on reduction of Fe_2O_3 by a low-temperature hydrogen plasma. High Temp Mater Process 20:317–332
23. Chen F, Mohassab Y, Zhang S, Sohn HY (2015) Kinetics of the reduction of hematite concentrate particles by carbon monoxide relevant to a novel flash ironmaking process. Metall Mater Trans B Process Metall Mater Process Sci 46:1716–1728. https://doi.org/10.1007/s11663-015-0345-7
24. Wang H, Sohn HY (2013) Hydrogen reduction kinetics of magnetite concentrate particles relevant to a novel flash ironmaking process. Metall Mater Trans B Process Metall Mater Process Sci 44:133–145. https://doi.org/10.1007/s11663-012-9754-z

25. Abolpour B, Afsahi MM, Soltani Goharrizi A, Azizkarimi M (2017) Investigation of in-flight reduction of magnetite concentrate by hydrogen. Ironmak Steelmak. https://doi.org/10.1080/03019233.2017.1405146

26. Rodriguez JA, Hanson JC, Frenkel AI et al (2002) Experimental and theoretical studies on the reaction of H_2 with NiO: role of O vacancies and mechanism for oxide reduction. J Am Chem Soc 124:346–354. https://doi.org/10.1021/ja0121080

27. Richardson JT, Scates R, Twigg MV (2003) X-ray diffraction study of nickel oxide reduction by hydrogen. Appl Catal A Gen 246:137–150

28. Jeangros Q, Hansen TW, Wagner JB et al (2013) Reduction of nickel oxide particles by hydrogen studied in an environmental TEM. J Mater Sci 48:2893–2907. https://doi.org/10.1007/s10853-012-7001-2

29. Rodriguez JA, Kim JY, Hanson JC et al (2003) Reduction of CuO in H_2: in situ time-resolved XRD studies. Catal Lett 85:247–254. https://doi.org/10.1023/A:1022110200942

30. Kim JY, Rodriguez A, Hanson JC et al (2003) Reduction of CuO and Cu_2O with H_2: H embedding and kinetic effects in the formation of suboxides. J Am Chem Soc 125:10684–10692

31. Cahn RW, Haasen P (1996) Physical metallurgy—vol 1. Phys Metall 1:1042. https://doi.org/10.1016/B978-0-444-89875-3.50041-7

32. Cahn RW, Haasen P (1996) Physical metallurgy—vol 2. Phys Metall 2:944. https://doi.org/10.1016/B978-0-444-89875-3.50041-7

33. Hassouni K, Gicquel A, Capitelli M, Loureiro J (1999) Chemical kinetics and energy transfer in moderate pressure H_2 plasmas used in diamond MPACVD processes. Plasma Sources Sci Technol 8:494–512. https://doi.org/10.1088/0963-0252/8/3/320

34. Piotrowski K, Mondal K, Wiltowski T et al (2007) Topochemical approach of kinetics of the reduction of hematite to wustite. Chem Eng J 131:73–82. https://doi.org/10.1016/j.cej.2006.12.024

35. Jacob KT, Raj S, Rannesh L (2007) Vegard's law: a fundamental relation or an approximation? Int J Mater Res 98:776–779. https://doi.org/10.3139/146.101545

36. Bindu P, Thomas S (2014) Estimation of lattice strain in ZnO nanoparticles: X-ray peak profile analysis. J Theor Appl Phys 8:123–134. https://doi.org/10.1007/s40094-014-0141-9

37. Cullity SR, Stock BD (2001) Elements of X-ray diffraction. Prentice-Hall, Englewood Cliffs

38. Suryanarayana C, Norton MG (1998) X-rays and diffraction. X-ray Diffr. https://doi.org/10.1007/978-1-4899-0148-4_1